

Factorization-free Orthogonal Projection onto the Positive Semidefinite Cone with Composite Polynomial Filtering

Shucheng Kang* Haoyu Han* Antoine Groudiev*[†] Heng Yang*[‡]

July 15, 2025

Abstract

We propose a factorization-free method for orthogonal projection onto the positive semidefinite (PSD) cone, leveraging composite polynomial filtering. Inspired by recent advances in homomorphic encryption, our approach approximates the PSD cone projection operator using a carefully optimized composite polynomial evaluated exclusively via matrix-matrix multiplications. This approach enables efficient GPU implementations with low-precision arithmetic, significantly outperforming the classical PSD cone projection using state-of-the-art GPU-based eigenvalue decomposition solvers. Specifically, our method achieves a consistent relative error of 10^{-3} in half-precision arithmetic with only 22 matrix-matrix multiplications, providing roughly a $10\times$ speed-up over NVIDIA’s `cuSOLVER` routines on various large-scale matrices. In single-precision arithmetic with emulation on B200 GPUs, our approach maintains competitive accuracy while achieving up to a $2\times$ speed-up. Consequently, for a $10,000 \times 10,000$ dense symmetric matrix, our method requires approximately 55 ms in half-precision and 400 ms in single-precision arithmetic on B200 GPUs. Integration into a first-order semidefinite programming solver confirms that our low-precision projections reliably yield solutions of moderate accuracy.

1 Introduction

Consider the classical problem of orthogonally projecting a symmetric matrix X onto the positive semidefinite (PSD) cone:

$$\Pi_{\mathbb{S}_+^n}(X) := \arg \min_{Y \in \mathbb{S}_+^n} \frac{1}{2} \|Y - X\|_F^2, \quad (1)$$

where \mathbb{S}^n denotes the space of $n \times n$ real symmetric matrices, $\mathbb{S}_+^n := \{A \in \mathbb{S}^n \mid A \succeq 0\}$ is the PSD cone, and $\|\cdot\|_F$ is the Frobenius norm. Computing this projection—yielding the nearest PSD approximation of X —is a fundamental primitive in numerous fields, including optimization [19, 43], signal processing [48], finance [16], machine learning [42], and quantum mechanics [3, 8]. In particular, it is invoked repeatedly to enforce feasibility in first-order algorithms for large-scale semidefinite programming (SDP) [10, 21, 33, 45, 47, 50].

Classical factorization-based solution. Suppose the spectral decomposition of X is given by

$$X = Q\Lambda Q^\top, \quad (2)$$

where $\Lambda = \text{diag}(\lambda_1, \dots, \lambda_n)$ is a diagonal matrix containing the n real eigenvalues of X , and $Q \in \mathbb{R}^{n \times n}$ is an orthonormal matrix whose columns are the corresponding eigenvectors. Higham [15] gave a closed-form solution to (1) as

$$\Pi_{\mathbb{S}_+^n}(X) = Q \text{diag}(\max\{\lambda_1, 0\}, \dots, \max\{\lambda_n, 0\}) Q^\top. \quad (3)$$

*School of Engineering and Applied Sciences, Harvard University. {skang1, hyhan, hankyang}@g.harvard.edu

[†]Computer Science Department, Ecole Normale Supérieure, PSL University. antoine.groudiev@ens.psl.eu

[‡]NVIDIA Corporation

Essentially, projecting X onto the PSD cone amounts to zeroing out its negative eigenvalues and corresponding eigenvectors. This insight naturally leads to using the eigenvalue decomposition (EVD) as the standard method for PSD cone projection. Due to its robustness and numerical reliability, full EVD has become the default routine for PSD cone projection and widely used in first-order SDP optimizers [21, 33, 42, 43, 48].

However, recent advances in numerical optimization—particularly first-order methods for solving large-scale SDPs derived from convex relaxations [13, 20–22, 26, 41, 45, 47]—require repeated projections onto the PSD cone for dense matrices with dimensions in the *tens of thousands* (i.e., $n \geq 10,000$ in (1)). As a result, classical projection via full EVD has become suboptimal for two reasons. First, the tridiagonalization phase of QR-factorization-based EVD is memory-bound [7, 12], limiting the ability to leverage high-throughput modern hardware such as the graphics processing unit (GPU) for acceleration. Second, high-precision projections (e.g., 64-bit machine precision) can be unnecessary in first-order methods, where standard termination criteria only require the Karush-Kuhn-Tucker (KKT) residual to fall below $10^{-2} \sim 10^{-4}$ [21, 33, 50]. Yet implementing EVD in lower precision (e.g., half precision on GPU Tensor Cores) remains difficult due to the strict orthogonality requirements intrinsic to factorization-based algorithms [46]. Therefore, the central motivation of this paper is:

Can we design an efficient, factorization-free algorithm for PSD cone projection that is compatible with low-precision arithmetic? Moreover, how much speedup can such an approach achieve compared to state-of-the-art GPU-based eigenvalue-decomposition solvers?

Factorization-free solution via polynomial filtering. A key step toward a factorization-free approach for PSD cone projection is recognizing that the closed-form solution (3) can be expressed as a *spectral operator* applied to X . Specifically, a spectral operator $F(X) : \mathbb{S}^n \rightarrow \mathbb{S}^n$ is said to be generated by a scalar function $f(x) : \mathbb{R} \rightarrow \mathbb{R}$ if $F(X)$ is equivalent to applying $f(x)$ to the eigenvalues of X [7], namely,

$$F(X) = Q \text{diag}(f(\lambda_1), \dots, f(\lambda_n)) Q^\top, \quad (4)$$

where X admits the spectral decomposition defined in (2). Under this framework, the PSD projection $\Pi_{\mathbb{S}_+^n}(X)$ corresponds to the spectral operator generated by the Rectified Linear Unit (ReLU): $f_{\text{ReLU}}(x) = \max\{x, 0\}$.

Building on this observation, one can approximate $f_{\text{ReLU}}(x)$ using a *polynomial* $p(x)$. The advantage of this approach is that it avoids explicit eigenvalue decomposition:

$$\Pi_{\mathbb{S}_+^n}(X) = Q \text{diag}(f_{\text{ReLU}}(\lambda_1), \dots, f_{\text{ReLU}}(\lambda_n)) Q^\top \approx Q \text{diag}(p(\lambda_1), \dots, p(\lambda_n)) Q^\top = p(X), \quad (5)$$

where the final equality follows from the fact that for any integer $d \in \mathbb{N}$,

$$X^d = \underbrace{(Q \text{diag}(\lambda_1, \dots, \lambda_n) Q^\top)(Q \text{diag}(\lambda_1, \dots, \lambda_n) Q^\top) \cdots (Q \text{diag}(\lambda_1, \dots, \lambda_n) Q^\top)}_{d \text{ times}} = Q \text{diag}(\lambda_1^d, \dots, \lambda_n^d) Q^\top.$$

Thus, a good polynomial approximation $p(x) \approx f_{\text{ReLU}}(x)$ enables PSD projection purely through general matrix-matrix multiplications (GEMM), making the method highly amenable to GPU acceleration [29, 30]. This technique is commonly referred to as *polynomial filtering* [9]. Under this paradigm, the central challenge becomes:

Given a fixed budget of GEMMs, how to construct an optimal polynomial $p(x)$ that best approximates $f_{\text{ReLU}}(x)$, and how to efficiently implement the resulting polynomial filter on GPUs?

It is worth noting that if $p(x)$ is allowed to span the full monomial basis up to degree d , then the best polynomial approximation to $f_{\text{ReLU}}(x)$ can be constructed efficiently [39, Theorem 10.1]. However, accurately approximating the nonsmooth $f_{\text{ReLU}}(x)$ requires high-degree polynomials, which in turn increases the number of GEMMs needed to evaluate the filter. As a result, such unstructured high-degree approximations are often too costly to compete with classical PSD projection via EVD in practice. To overcome this limitation, we need to seek a *structured* high-order polynomial $p(x)$ that achieves a good trade-off between approximation quality and computational efficiency—i.e., one that can be implemented using only a small number of GEMMs.

Contribution. Inspired by recent work in homomorphic encryption on approximating the *sign function* [25], we propose a *composite polynomial filter* for approximating $f_{\text{ReLU}}(x)$. The idea is to express the polynomial approximation as a composition of T low-degree polynomials:

$$p(x) = f_T \circ f_{T-1} \circ \dots \circ f_1(x), \quad (6)$$

where each f_i , for $i \in [T]$, is a polynomial of degree at most d_i . By construction, the total degree of $p(x)$ is $\prod_{i=1}^T d_i$, yet the composite structure enables its evaluation using only $\sum_{i=1}^T d_i$ GEMMs. This approach thus enables high-degree (and more accurate) approximations at a significantly reduced computational cost, making it well-suited for efficient GPU implementation.

We contribute (i) an algorithmic framework for optimizing composite polynomial coefficients to minimize the worst-case approximation error of $f_{\text{ReLU}}(x)$, and (ii) a high-performance GPU implementation of the resulting filter that outperforms classical factorization-based PSD projection. Specifically:

1. **Optimization of polynomial coefficients.** To minimize the worst-case approximation error under a fixed budget of GEMMs, we introduce a two-stage framework for designing the composite polynomial filter:
 - (i) *Minimax initialization.* We construct a sequence of composite polynomials that approximate the matrix sign function—a surrogate for the ReLU function. The coefficients of each low-degree component are computed via the Remez algorithm [35], following the approach in [25]. The obtained composite polynomials are proven to be minimax optimal for the sign function under mild conditions.
 - (ii) *Gradient-based refinement.* Since the minimax approximation is tailored to the sign function and not directly to $f_{\text{ReLU}}(x)$, we further refine the coefficients using gradient descent. This step treats the polynomial coefficients as unconstrained, non-convex optimization variables, directly targeting approximation of $f_{\text{ReLU}}(x)$. The refinement further reduces error beyond the initial minimax stage.

As a result of the two-stage optimization, our method achieves a lower approximation error with the same number of GEMMs compared to prior polynomial filtering approaches for PSD projection [9].

2. **GPU implementation and performance evaluation.** We implemented the composite polynomial filter in native C++ and CUDA, leveraging Tensor Cores and BF16x9 emulation techniques [32] to achieve high computational efficiency. We benchmarked our method on both NVIDIA B200 and NVIDIA H100 GPUs, comparing its performance against the commercial cuSOLVER library [31] and previous polynomial filtering approaches [1, 9]. In half-precision arithmetic, our filter consistently attains a relative error of approximately 10^{-3} using only 22 GEMM operations across diverse large-scale matrix datasets. This results in a stable speed-up of approximately $10\times$ compared to cuSOLVER’s eigenvalue decomposition (EVD). For single-precision arithmetic, with emulation enabled on the B200 GPU, our polynomial filter achieves up to $2\times$ speed-up over cuSOLVER’s single-precision EVD implementation while utilizing 31 GEMM launches, and it maintains comparable accuracy. Furthermore, when integrated into a first-order SDP solver, our lower-accuracy projection method remains effective, allowing the solver to reliably converge to solutions of moderate accuracy.

Our PSD cone projection package based on composite polynomial filtering is open-sourced at

https://github.com/ComputationalRobotics/psd_projection.

Outline. Related work is reviewed in Section 2. Section 3 introduces our composite polynomial filter design framework. Implementation details and experimental results are presented in Section 4, followed by conclusions in Section 5.

2 Related Work

PSD cone projection via eigenvalue decomposition. Eigenvalue decomposition is often employed to obtain Q and $\{\lambda_i\}_{i=1}^n$ in (3). In general, the full decomposition of an $n \times n$ dense symmetric matrix X has computational complexity $\mathcal{O}(n^3)$ and memory complexity $\mathcal{O}(n^2)$ and is widely implemented across various computing architectures [2, 31, 38]. Almost all existing first-order SDP solvers rely on full eigenvalue decomposition for PSD cone projection [10, 21, 33, 47, 50]. When either the positive or negative eigenvalue component is low-rank, PSD cone projection can be accelerated using low-rank eigenvalue decomposition algorithms [36]. Sketching- and randomization-based methods for approximate large-scale PSD cone projection also exist [18], but their convergence guarantees hold only in a probabilistic sense. All these methods explicitly rely on knowledge of (at least some) eigenvalue-eigenvector pairs.

Matrix sign function approximation via polynomial/rational fixed point iteration. Let X admit the spectral decomposition in (2), the matrix sign function is defined as [6]

$$f_{\text{sign}}(X) := Q \text{diag}(f_{\text{sign}}(\lambda_1), \dots, f_{\text{sign}}(\lambda_n)) Q^T, \quad (7)$$

where $f_{\text{sign}}(\cdot)$ is defined in (10). A substantial body of literature has developed polynomial- and rational-based fixed-point schemes for computing the matrix sign function, including the Newton iteration [14, 17], the inverse Newton iteration [28], and several Newton–Schulz variants [5, 51]. These methods involve only matrix-matrix multiplications or matrix inversions, making them more suitable for large-scale parallel architectures where the computational and communication overhead of full eigenvalue decomposition quickly becomes prohibitive. In the context of PSD cone projection, [9] proposed rewriting (3)—the spectral operator generated by $f_{\text{ReLU}}(x)$ —as $0.5X(I + f_{\text{sign}}(X))$ and employed a variant of the Newton–Schulz iteration to approximate the matrix sign function, primarily targeting PSD projection of sparse, banded matrices. However, while fixed-point iterations can achieve local quadratic convergence given knowledge of the smallest absolute eigenvalue [9], in practice, achieving even moderate accuracy typically requires many iterations [5], thus diminishing their speed advantage relative to full eigenvalue decomposition. In optimization of neural networks, [1] recently employed a sequence of degree-5 minimax composite polynomials to approximate the polar factor (a generalization of matrix sign function) at low accuracy. Nevertheless, the GPU-level competitiveness of such composite polynomial filtering, relative to state-of-the-art factorization-based approaches, remains unclear.

Background for GPU computation. GPU math libraries organize kernels using the BLAS hierarchy: Level-2 routines (matrix-vector) involve $\mathcal{O}(n^2)$ floating-point operations and $\mathcal{O}(n^2)$ data movement, yielding low arithmetic intensity; Level-3 routines (matrix-matrix) perform $\mathcal{O}(n^3)$ work for the same $\mathcal{O}(n^2)$ memory traffic, achieving far higher intensity [32]. Under the Roofline model [44], this means Level-2 kernels are typically memory-bound while Level-3 kernels can become compute-bound once their arithmetic intensity exceeds the machine’s balance point. Empirical studies confirm that large-scale GEMM kernels on modern GPUs routinely sustain over 90% of peak compute throughput, making them archetypal compute-bound workloads [40]. In contrast, dense eigenvalue decomposition (EVD) begins with a reduction to (banded) tridiagonal form dominated by BLAS-2 updates; because these updates are memory-bound, the end-to-end EVD pipeline is usually limited by memory bandwidth even though it contains some compute-heavy BLAS-3 sweeps. Furthermore, modern GPUs such as NVIDIA’s Ampere A100 incorporate Tensor Cores—specialized mixed-precision matrix-multiply-accumulate (MMA) units that push peak throughput beyond 300 TFLOP/s in half precision and deliver orders-of-magnitude speedups for dense linear-algebra kernels compared to general CUDA cores [29]. This further amplifies BLAS-3 operator’s advantage over BLAS-2 operator.

3 Composite Polynomial Filter Design

In this section we present a two-stage framework that efficiently approximates $f_{\text{ReLU}}(x)$ with a sequence of low-degree polynomials combined through addition, multiplication, and composition.

Minimax formulation for $f_{\text{ReLU}}(x)$. Recall from Section 1 that the goal is to find a composite polynomial filter, in the form of (6), that best approximates $f_{\text{ReLU}}(x)$. To do so, we adopt the classical minimax criterion from approximation theory [39, Chapter 10]:

$$\begin{aligned} \inf_{f_1, \dots, f_T} \max_{x \in [-1, 1]} |f_T \circ f_{T-1} \circ \dots \circ f_1(x) - f_{\text{ReLU}}(x)| \\ \text{subject to} \quad f_t \in \mathbb{R}_{d_t}[x], \quad t = 1, \dots, T. \end{aligned} \quad (8)$$

Here the total number of polynomials T and their degrees $\{d_t\}_{t=1}^T$ are fixed in advance as the computational budget. The set $\mathbb{R}_{d_t}[x]$ includes real (univariate) polynomials of degree at most d_t . Restricting x to $[-1, 1]$ does not result in loss of generality, as we can efficiently rescale the matrix X so that its eigenvalues lie in this interval. Since the minimax optimality under composition may not be attainable [11], we use “inf” in (8). Let $D := \prod_{t=1}^T d_t$ be the degree of the composite polynomial filter.

Challenges. Directly solving (8) is challenging, even under the assumption that the minimax optimum of the composite structure is attainable. Classical approximation tools such as Chebyshev criteria and the Remez algorithm [35] are not applicable, as the composite polynomial $f_T \circ \dots \circ f_1(x)$ does not span the full polynomial space $\mathbb{R}_D[x]$. While global optimization techniques—such as the two-level semidefinite relaxation hierarchy for robust polynomial optimization [24]—can, in principle, solve (8), they face severe scalability limitations due to the high polynomial degrees involved.

Two-stage design strategy. To address these challenges, we adopt a two-stage design strategy to approximately solve (8). In Stage I (Section 3.1), we construct a minimax-optimal composite polynomial approximation for the surrogate function $f_{\text{sign}}(x)$. In Stage II (Section 3.2), we locally refine the polynomials obtained in Stage I using the true minimax objective for $f_{\text{ReLU}}(x)$ in (8).

3.1 Stage I: Minimax Composite Polynomials for $f_{\text{sign}}(x)$

Minimax formulation for $f_{\text{sign}}(x)$. A growing body of evidence shows that approximating $f_{\text{sign}}(x)$ with polynomial compositions is far more tractable [1, 5, 9, 25]. Consider

$$\begin{aligned} \{f_t^*\}_{t=1}^T = \arg \min_{f_1, \dots, f_T} \max_{x \in [-1, -\epsilon] \cup [\epsilon, 1]} |f_T \circ f_{T-1} \circ \dots \circ f_1(x) - f_{\text{sign}}(x)| \\ \text{subject to} \quad f_t \in \mathbb{R}_{d_t}^{\text{odd}}[x], \quad t = 1, \dots, T, \end{aligned} \quad (9)$$

where $\epsilon \in (0, 1)$ is a tunable hyperparameter to address the discontinuity issue when approximating $f_{\text{sign}}(x)$, $\mathbb{R}_{d_t}^{\text{odd}}[x]$ represents the subspace of $\mathbb{R}_{d_t}[x]$ containing all odd polynomials, and

$$f_{\text{sign}}(x) := \begin{cases} 1, & x > 0, \\ 0.5, & x = 0, \\ -1, & x < 0, \end{cases} \quad \text{with} \quad f_{\text{ReLU}}(x) = \frac{1}{2}x(1 + f_{\text{sign}}(x)). \quad (10)$$

We only consider odd polynomials in (9) since $f_{\text{sign}}(x)$ is an odd function. [25, Definition 7] proposes an efficient greedy algorithm to solve (9), presented in Algorithm 1. In there, (11) holds since f_{sign} and f are both odd. Remez($g, [a, b], \Phi$) in (12) is used to determine the unique minimax approximate polynomial for a continuous function g over interval $[a, b]$ with basis Φ . Over the iterations, a_t remains positive. Thus,

$\mathbb{R}_{d_t}^{\text{odd}}[x]$ satisfies the Haar condition on $[a_t, b_t]$ and the Remez algorithm converges [1, Lemma A.1]. We defer the detailed discussion for the Remez algorithm to Appendix A. The next Theorem states the correctness of Algorithm 1.

Algorithm 1: A sequential Remez algorithm to solve (9)

Input: Composite step T , degrees $\{d_t\}_{t=1}^T$, hyperparameter ϵ .

Output: Minimax composite polynomials $\{f_t^*\}_{t=1}^T$ for (9).

1 Initialization: $a_t \leftarrow \epsilon$, $b_t \leftarrow 1$.

2 **for** $t = 1$ to T **do**

3 (1) Choose a basis Φ_t of $\mathbb{R}_{d_t}^{\text{odd}}[x]$. f_t^* is the minimax approximate polynomial of degree at most d_t for f_{sign} over $[-b_t, -a_t] \cup [a_t, b_t]$:

$$\begin{aligned} f_t^* &:= \arg \min_{f \in \mathbb{R}_{d_t}^{\text{odd}}[x]} \max_{x \in [-b_t, -a_t] \cup [a_t, b_t]} |f(x) - f_{\text{sign}}(x)| \\ &= \arg \min_{f \in \mathbb{R}_{d_t}^{\text{odd}}[x]} \max_{x \in [a_t, b_t]} |f(x) - f_{\text{sign}}(x)| \end{aligned} \quad (11)$$

$$\leftarrow \text{Remez}(f_{\text{sign}}, [a_t, b_t], \Phi_t). \quad (12)$$

4 (2) Set the $(t+1)$ 'th interval $[a_{t+1}, b_{t+1}]$ as the image of $[a_t, b_t]$ under f_t^* :

$$[a_{t+1}, b_{t+1}] \leftarrow f_t^*([a_t, b_t]). \quad (13)$$

5 **end**

Theorem 1 (Minimax Optimality). *Given the composite step T , degrees $\{d_t\}_{t=1}^T$, and hyperparameter ϵ , $\{f_t^*\}_{t=1}^T$ generated by Algorithm 1 is minimax optimal for (9).*

Theorem 1 can be directly deduced from [25, Theorem 2]. [1, Theorem 4.1] also provides an independent proof. We provide the proof here for completeness.

Proof for Theorem 1. Prove by contradiction. Denote $\{f_t^*\}_{t=1}^T$ as the polynomial sequence generated by Algorithm 1. Its approximation error is: $E^* = \max_{x \in [\epsilon, 1]} |f_T^* \circ f_{T-1}^* \circ \dots \circ f_1^*(x) - f_{\text{sign}}(x)|$. Now suppose (9)'s optimal minimax value $E_{\min} < E^*$. Invoking [25, Theorem 2], there exists a polynomial sequence $\{w_t\}_{t=1}^T$ generated by Algorithm 1, such that $E_{\min} \geq \max_{x \in [\epsilon, 1]} |w_T \circ w_{T-1} \circ \dots \circ w_1(x) - f_{\text{sign}}(x)|$. On the other hand, the uniqueness of each Remez algorithm step in (12) under Haar condition is guaranteed. Thus, $w_1 = f_1^*, w_2 = f_2^*, \dots, w_T = f_T^*$, which leads to the contradiction. \square

3.2 Stage II: Gradient-based Refinement for $f_{\text{ReLU}}(x)$

Given an approximation sequence $\{f_t^*\}_{t=1}^T$ to $f_{\text{sign}}(x)$, an approximation to $f_{\text{ReLU}}(x)$ follows immediately:

$$f_{\text{ReLU}}(x) \approx \frac{1}{2}x(1 + f_T^* \circ f_{T-1}^* \circ \dots \circ f_1^*(x)) =: f^*(x). \quad (14)$$

However, even if $f_T^* \circ f_{T-1}^* \circ \dots \circ f_1^*(x)$ is minimax-optimal for (9), there is no guarantee that the resulting $f^*(x)$ is minimax-optimal for (8). Following the coefficient-refinement strategy of [4], we carry out an additional gradient-based local optimization of the coefficients, exploiting modern automatic-differentiation toolchains. Concretely, we minimize the loss function

$$\ell(f_T, \dots, f_1) := \max_{x \in [-1, 1]} \left| \frac{1}{2}x(1 + f_T \circ f_{T-1} \circ \dots \circ f_1(x)) - f_{\text{ReLU}}(x) \right|, \quad (15)$$

evaluating it on a dense set of sample points in the interval $[-1, 1]$. The weights of $\{f_t\}_{t=1}^T$ are initialized with the coefficients of $\{f_t^*\}_{t=1}^T$ (computed from Stage I) and are then progressively refined by gradient descent. Once this optimization converges, we denote the resulting composite polynomial by

$$\tilde{f}^*(x) := \frac{1}{2} x \left(1 + \tilde{f}_T^* \circ \tilde{f}_{T-1}^* \circ \cdots \circ \tilde{f}_1^*(x) \right). \quad (16)$$

Approximation error evaluation. Given an arbitrary composite function f , it is difficult to obtain the exact approximation error in the ∞ -norm, $e(f) := \max_{x \in [-1, 1]} |f(x) - f_{\text{ReLU}}(x)|$. Since our implementation ultimately targets single- or even half-precision arithmetic, it is practically sufficient to evaluate the point-wise error at every single-precision representable value in $[-1, 1]$. The complete set of such points, denoted S_{float} , contains 2,130,706,433 elements. We therefore work with and evaluate the discretized error

$$e_{\text{float}}(f) := \max_{x_i \in S_{\text{float}}} |f(x_i) - f_{\text{ReLU}}(x_i)|. \quad (17)$$

Although $e_{\text{float}}(f)$ is merely an approximation of $e(f)$, our extensive benchmarking of PSD-cone projections (cf. § 4.1) clearly demonstrates the practical benefits of our refined coefficients.

3.3 Explicit Formulations of Composite Polynomial Filters

Integrating the techniques outlined above, we design two composite-polynomial variants, each tailored to single- and half-precision settings, respectively. Guided by the principles in [1, 25], we set $d_t = 5$ for all t .

(1) *Single precision setting.* We set $\epsilon = 10^{-3}$, $T = 10$. $\{f_t^*\}_{t=1}^T$, $\{\tilde{f}_t^*\}_{t=1}^T$, and their corresponding e_{float} are listed in Table 1. The final $\tilde{f}_{\text{single}}^*$ involves 31 GEMMs.

| | f_{single}^* | $\tilde{f}_{\text{single}}^*$ |
|--------------------|---|---|
| formula | $f_1^*(x) = 8.5098853026x - 25.2643041908x^3 + 18.7535678997x^5$ | $\tilde{f}_1^*(x) = 8.3119043343x - 23.0739115930x^3 + 16.4664144722x^5$ |
| | $f_2^*(x) = 4.2495734789x - 3.1549764881x^3 + 0.5858847825x^5$ | $\tilde{f}_2^*(x) = 4.1439360087x - 2.9176674704x^3 + 0.5246212487x^5$ |
| | $f_3^*(x) = 4.2251221908x - 3.1380444351x^3 + 0.5839534551x^5$ | $\tilde{f}_3^*(x) = 4.0257813209x - 2.9025002398x^3 + 0.5334261214x^5$ |
| | $f_4^*(x) = 4.1248386870x - 3.0683324528x^3 + 0.5760029536x^5$ | $\tilde{f}_4^*(x) = 3.5118574347x - 2.5740236523x^3 + 0.5050097282x^5$ |
| | $f_5^*(x) = 3.7580103358x - 2.8092738924x^3 + 0.5464842066x^5$ | $\tilde{f}_5^*(x) = 2.4398158400x - 1.7586675341x^3 + 0.4191290613x^5$ |
| | $f_6^*(x) = 2.8561775413x - 2.1340562332x^3 + 0.4701107692x^5$ | $\tilde{f}_6^*(x) = 1.9779835097x - 1.3337358510x^3 + 0.3772169049x^5$ |
| | $f_7^*(x) = 2.0206004158x - 1.4037211505x^3 + 0.3906738969x^5$ | $\tilde{f}_7^*(x) = 1.9559726949x - 1.3091355170x^3 + 0.3746734515x^5$ |
| | $f_8^*(x) = 1.8758751005x - 1.2509719905x^3 + 0.3750972123x^5$ | $\tilde{f}_8^*(x) = 1.9282822454x - 1.2823649693x^3 + 0.3704626545x^5$ |
| | $f_9^*(x) = 1.8750000000x - 1.2500000000x^3 + 0.3750000000x^5$ | $\tilde{f}_9^*(x) = 1.9220135179x - 1.2812524618x^3 + 0.3707011753x^5$ |
| | $f_{10}^*(x) = 1.8750000000x - 1.2500000000x^3 + 0.3750000000x^5$ | $\tilde{f}_{10}^*(x) = 1.8942192942x - 1.2613293407x^3 + 0.3676616051x^5$ |
| e_{float} | 1.1092×10^{-5} | 8.7023×10^{-6} |

Table 1: Composite polynomials for single-precision PSD cone projection.

(2) *Half precision setting.* We set $\epsilon = 10^{-3}$, $T = 7$. $\{f_t^*\}_{t=1}^T$, $\{\tilde{f}_t^*\}_{t=1}^T$, and their corresponding e_{float} are listed in Table 2. The final $\tilde{f}_{\text{half}}^*$ involves 22 GEMMs.

3.4 Practical Considerations for Finite-Precision Implementation

When porting \tilde{f}^* to GPUs that operate in single- or half-precision, two practical issues arise.

1. Digit loss during matrix rescaling. Before applying \tilde{f}^* to a matrix $X \in \mathbb{S}^n$, we rescale its spectrum to lie in $[-1, 1]$, dividing X by an upper bound on its spectral norm $\|X\|_2$. A common choice is the Frobenius norm $\|X\|_F$ [1] or the infinity norm $\|X\|_\infty$ [9]. However, since

$$\|X\|_2 \leq \|X\|_F \leq \sqrt{n} \|X\|_2, \quad \|X\|_2 \leq \|X\|_\infty \leq \sqrt{n} \|X\|_2,$$

| | f_{half}^* | $\tilde{f}_{\text{half}}^*$ |
|--------------------|--|--|
| formula | $f_1^*(x) = 8.4703288038x - 25.1080747067x^3 + 18.6292755991x^5$ | $\tilde{f}_1^*(x) = 8.2885332412x - 22.5927099246x^3 + 15.8201383114x^5$ |
| | $f_2^*(x) = 4.1828341833x - 3.1087011099x^3 + 0.5806066814x^5$ | $\tilde{f}_2^*(x) = 4.1666196466x - 2.9679004036x^3 + 0.5307623217x^5$ |
| | $f_3^*(x) = 3.9618572790x - 2.9540637464x^3 + 0.5629761180x^5$ | $\tilde{f}_3^*(x) = 4.0611848147x - 2.9698947955x^3 + 0.5492133813x^5$ |
| | $f_4^*(x) = 3.2865862170x - 2.4647201345x^3 + 0.5073576939x^5$ | $\tilde{f}_4^*(x) = 3.6678301399x - 2.7561018955x^3 + 0.5421513305x^5$ |
| | $f_5^*(x) = 2.2737499945x - 1.6446603679x^3 + 0.4161909275x^5$ | $\tilde{f}_5^*(x) = 2.7632556383x - 2.0607754898x^3 + 0.4695405857x^5$ |
| | $f_6^*(x) = 1.8887161973x - 1.2651572253x^3 + 0.3765189256x^5$ | $\tilde{f}_6^*(x) = 2.0527445797x - 1.4345145882x^3 + 0.4070669182x^5$ |
| | $f_7^*(x) = 1.8750008858x - 1.2500009843x^3 + 0.3750000984x^5$ | $\tilde{f}_7^*(x) = 1.8804816691x - 1.2583997294x^3 + 0.3779501813x^5$ |
| c_{float} | 7.2868×10^{-5} | 4.9233×10^{-5} |

Table 2: Composite polynomials for half-precision PSD cone projection.

for $n \geq 10,000$ these conservative bounds can cost the loss of $\log_{10}(\sqrt{n}) \geq 2$ decimal digits in the worst case. To tighten the bound, we adopt the following result, derived from the Residual Norm Theorem [34, Theorem 4.5.1].

Theorem 2 (Tighter upper bound for $\|A\|_2$). *Let $A \in \mathbb{S}^n$ and let $0 \leq \lambda_n \leq \dots \leq \lambda_1$ be the eigenvalues of A^2 . Fix $\sigma \in \mathbb{R}$ and assume λ_1 is the eigenvalue of A^2 closest to σ (i.e. $\lambda_1 = \arg \min_{\lambda_i} |\sigma - \lambda_i|$). Then, for every unit vector $q \in \mathbb{R}^n$,*

$$\|A\|_2 \leq \sqrt{\sigma + \|A^2 q - \sigma q\|_2}. \quad (18)$$

Proof. From [34, Theorem 4.5.1, Proof 2],

$$|\lambda_1 - \sigma| \leq \|A^2 q - \sigma q\|_2. \quad (19)$$

Because $\|A\|_2 = \sqrt{\|A^2\|_2} = \sqrt{\lambda_1}$, the claim follows. \square

In practice, we choose (σ, q) by taking the largest Ritz value produced by a 20-step Lanczos [34, Chapter 13] run on A^2 together with its Ritz vector. Although the theorem assumes σ is the closest to $\lambda_{\max}(A^2)$, we have found this heuristic to yield a valid upper bound in all our extensive experiments. Since Lanczos iterations only involves matrix-vector multiplications, its running time is negligible compared to GEMMs.

2. Numerical instability. As noted in [1, Section 4.4], minimax composite polynomials can be unstable in half-precision. Following their rescaling strategy, we multiply X by $\frac{1}{1.01}$ at the end of every half-precision iteration. For single precision, we rescale by $\frac{1}{1.001}$ after each of the first eight iterations.

Final run-time algorithm. Given the composite polynomials coefficients computed offline, we implement the run-time algorithm in Algorithm 2. The first part computes the upper bound of $\|X\|_2$ using Theorem 2, and the second part iteratively applies the composite polynomial filter $\tilde{f}_T^* \circ \tilde{f}_{T-1}^* \circ \dots \circ \tilde{f}_1^*$ to X after scaling. The approximation of the projection $\Pi_{\mathbb{S}_+^n}(X)$ is then recovered by reconstructing $f_{\text{ReLU}}(X)$ from $f_{\text{sign}}(X)$ and unscaling the result.

4 Implementation and Evaluation

We implemented all algorithms in native C++ and CUDA, including the matrix-rescaling routine based on Lanczos iterations and the evaluation of composite matrix polynomials. The resulting codebase was benchmarked both on NVIDIA B200 GPUs (192 GB RAM) running CUDA 12.9 and on NVIDIA H100 GPUs (80 GB RAM) running CUDA 12.4. On the B200, we enabled the newest BF16x9 emulation features introduced in CUDA 12.9 for the Blackwell architecture, yielding significantly faster single-precision general GEMMs [32]. All Lanczos iterations are executed on the general CUDA cores in double precision (FP64),

Algorithm 2: Run-time projection algorithm to compute (1)

Input: Symmetric matrix X , composite step T , polynomials $\{\tilde{f}_t^*\}_{t=1}^T$.

Output: Approximation of the projection of X onto the PSD cone $\Pi_{\mathbb{S}_+^n}(X)$.

- 1 Compute the largest Ritz value pair (σ, q) with a 20-step Lanczos run on X^2 .
- 2 Compute the upper bound of $\|X\|_2$:

$$\tilde{\lambda} \leftarrow \sqrt{\sigma + \|X^2 q - \sigma q\|_2}. \quad (20)$$

- 3 Rescale X :

$$X_0 \leftarrow X / \tilde{\lambda} \quad (21)$$

- 4 **for** $t = 1$ to T **do**

- 5 Compute:

$$X_t \leftarrow \tilde{f}_t^*(X_{t-1}). \quad (22)$$

- 6 **end**

- 7 **return** $\tilde{\lambda} \cdot \frac{1}{2} X(I_n + X_T)$
-

mitigating the rapid loss of orthogonality. For composite matrix polynomials, we evaluate $\tilde{f}_{\text{half}}^*$ (cf. Table 2) on the Tensor Cores in half precision (FP16). In the case of $\tilde{f}_{\text{single}}^*$ (cf. Table 1), single precision (FP32) is employed on the H100’s CUDA cores, whereas on the B200 we leverage Tensor Core FP32 with emulation enabled. In terms of memory, our composite polynomial implementations require a workspace equivalent to the size of three additional matrices only. We use the state-of-the-art commercial CUDA library **cuSOLVER** for the FP64 and FP32 eigenvalue decomposition on GPUs.

4.1 Benchmarking PSD Cone Projection

Datasets. We evaluate the performance of the proposed method on 33 dense datasets from the Matrix Depot package [49]. Out of the 56 datasets available in the package, we removed 23 datasets of which the coefficients would overflow the double precision floating point representation for large matrix sizes, as well as datasets with constraints on the matrix size (e.g., the size being a power of 2). For each of the remaining 33 datasets, we generated 3 instances, of sizes 5000, 10000 and 20000. The matrices were symmetrized by averaging the matrix with its transpose ($A_{\text{sym}} = \frac{1}{2}(A + A^T)$).

Benchmark methods and metrics. We restrict our benchmarks exclusively to GPUs, as CPU-based projection methods are not competitive for large-scale problems. For example, on a $10,000 \times 10,000$ dense symmetric matrix, MATLAB’s **eig** function requires approximately 15 seconds on a high-performance workstation equipped with a 64-Core Processor, whereas NVIDIA’s **cuSOLVER** completes the eigenvalue decomposition in about 1 second on both B200 and H100 GPUs. We systematically compare nine methods:

- **cuSOLVER FP64:** classical factorization-based method with **cuSOLVER**. We also use this method as a ground truth for the PSD projection in the error metric.
- **cuSOLVER FP32:** same as **cuSOLVER FP64**, single precision.
- **Polar Express FP32:** composite coefficients proposed in [1] and implemented in FP32. We set $\ell = 10^{-3}$ and $T = 10$, resulting in 31 GEMMs.
- **Polar Express FP16:** composite coefficients proposed in [1] and implemented in FP16. We set $\ell = 10^{-3}$ and $T = 7$, resulting in 22 GEMMs.
- **Newton-Schulz FP32:** 15 Newton-Schulz iterations [9] implemented in FP32, resulting in 31 GEMMs.
- **Newton-Schulz FP16:** 10 Newton-Schulz iterations [9] implemented in FP16, resulting in 21 GEMMs.
- **Composite FP32:** the proposed method ($\tilde{f}_{\text{single}}^*$) in FP32 with 31 GEMMs.

- **Composite FP32 (em.)**: same as **Composite FP32**, with BF16x9 emulation enabled on B200 GPU.
- **Composite FP16**: the proposed method ($\tilde{f}_{\text{half}}^*$) in FP16 with 22 GEMMs.

We evaluate the performance of the methods using two metrics: *time* and *relative error*. The time includes both Lanczos iterations, data type conversion, and composite polynomial filtering. Given the input matrix $A \in \mathbb{S}^n$, denote an algorithm’s output matrix as A_+ . The relative error is defined as

$$\frac{\|A_+ - \Pi_{\mathbb{S}_+^n}(A)\|_F}{\|\Pi_{\mathbb{S}_+^n}(A)\|_F},$$

where $\Pi_{\mathbb{S}_+^n}(A)$ is from **cuSOLVER FP64**. The relative error is computed in **FP64**, regardless of the data type used for the PSD projection. For the same matrix, both metrics are averaged over 5 runs. The code used for the benchmarks is available at:

https://github.com/ComputationalRobotics/psd_projection_benchmarks.

Results. A synthetic view of the evaluation results on the B200 GPU is presented in Figure 1 and 2, with complementary statistics summarized in Tables 3, 4, and 5. Detailed, dataset-specific results for both B200 and H100 GPUs are provided in Appendix B. In terms of relative error, our proposed composite methods consistently outperform the other factorization-free approaches of their respective precisions, namely Polar Express [1] and Newton-Schulz [9]. In **FP16**, **Composite FP16** reliably achieves 10^{-3} relative error across a wide range of datasets while offering more than an order-of-magnitude speed-up over both **cuSOLVER FP64** and **cuSOLVER FP32**. Even for large dense matrices with $n = 20000$, it is able to finish projection within 300ms. In **FP32**, although **cuSOLVER FP32** generally attains the highest accuracy, **Composite FP32** (with emulation) can achieve speed-ups of up to $2\times$. As already noticeable from Figure 2, there are several datasets (e.g., the **triv** dataset) on which all composite methods perform poorly. A common characteristic of these matrices is the presence of one dominant extremal eigenvalue accompanied by many small but nonzero eigenvalues. As recommended in [34], applying a deflation technique to first remove the extremal eigenpairs could significantly improve performance in such cases.

Remark 1. We emphasize that the composite baseline methods from *Polar Express* and *Newton-Schulz* implemented here are already considerably improved compared to their original formulations [1, 9], due to our tighter spectral norm outer approximations described in § 3.4.

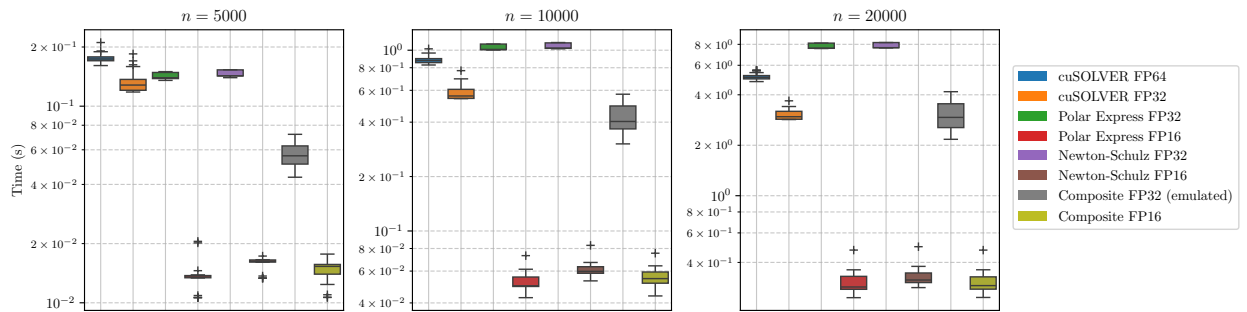


Figure 1: Boxplots for different PSD cone projection methods’ *execution time* on B200 GPU.

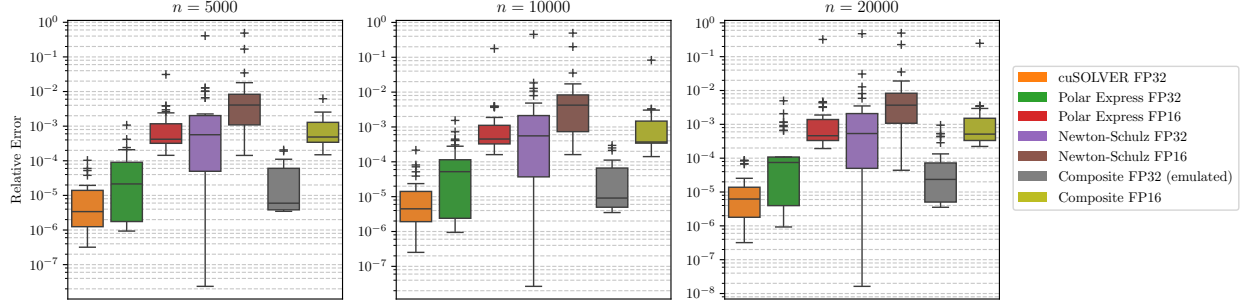


Figure 2: Boxplots for different PSD cone projection methods' *relative error* on B200 GPU.

| | Relative Error | | | Mean | Time (s) | |
|----------------------|-----------------------|-----------------------|-----------------------|-----------------------|-----------------------|-----------------------|
| | Mean | Median | Std. | | Median | Std. |
| cuSOLVER FP64 | 0.00×10^0 | 0.00×10^0 | 0.00×10^0 | 1.75×10^{-1} | 1.74×10^{-1} | 1.03×10^{-2} |
| cuSOLVER FP32 | 1.25×10^{-5} | 3.40×10^{-6} | 2.18×10^{-5} | 1.32×10^{-1} | 1.28×10^{-1} | 1.63×10^{-2} |
| Polar Express FP32 | 9.16×10^{-5} | 2.14×10^{-5} | 1.98×10^{-4} | 1.43×10^{-1} | 1.40×10^{-1} | 5.47×10^{-3} |
| Polar Express FP16 | 1.83×10^{-3} | 4.19×10^{-4} | 5.36×10^{-3} | 1.37×10^{-2} | 1.37×10^{-2} | 1.99×10^{-3} |
| Newton-Schulz FP32 | 1.47×10^{-2} | 5.65×10^{-4} | 7.07×10^{-2} | 1.47×10^{-1} | 1.43×10^{-1} | 5.56×10^{-3} |
| Newton-Schulz FP16 | 2.56×10^{-2} | 4.07×10^{-3} | 8.79×10^{-2} | 1.60×10^{-2} | 1.62×10^{-2} | 1.00×10^{-3} |
| Composite FP32 (em.) | 3.71×10^{-5} | 5.96×10^{-6} | 5.28×10^{-5} | 5.59×10^{-2} | 5.59×10^{-2} | 7.36×10^{-3} |
| Composite FP16 | 9.53×10^{-4} | 4.86×10^{-4} | 1.16×10^{-3} | 1.48×10^{-2} | 1.53×10^{-2} | 1.67×10^{-3} |

Table 3: Statistics of the PSD projection methods on datasets of size 5000 for B200 GPU.

4.2 Integration into Semidefinite Programming

ADMM for SDP. We further assess our low-precision composite PSD-cone projection by embedding it in a first-order solver for the semidefinite programming:

$$\begin{aligned}
 \text{Primal:} \quad & \text{minimize} \quad \langle C, X \rangle \\
 & \text{subject to} \quad \mathcal{A}X = b \\
 & \quad \quad \quad X \in \mathbb{S}_+^n \\
 \text{Dual:} \quad & \text{maximize} \quad b^\top y \\
 & \text{subject to} \quad \mathcal{A}^*y + S = C \\
 & \quad \quad \quad S \in \mathbb{S}_+^n,
 \end{aligned} \tag{23}$$

where the linear map $\mathcal{A} : \mathbb{S}^n \rightarrow \mathbb{R}^m$ is defined by $\mathcal{A}X := (\langle A_1, X \rangle, \dots, \langle A_m, X \rangle)$ and its adjoint $\mathcal{A}^*y = \sum_{i=1}^m y_i A_i$. We assume the matrices $\{A_i\}_{i=1}^m$ are linearly independent. Problem (23) is solved with the three-step Alternating Direction Method of Multipliers (ADMM) scheme from [19, 43]:

$$y^{(k+1)} = (\mathcal{A}\mathcal{A}^*)^{-1} \left(\sigma^{-1}b - \mathcal{A}(\sigma^{-1}X^{(k)} + S^{(k)} - C) \right), \tag{24a}$$

$$S^{(k+1)} = \Pi_{\mathbb{S}_+^n} \left(C - \mathcal{A}^*y^{(k+1)} - \sigma^{-1}X^{(k)} \right), \tag{24b}$$

$$X^{(k+1)} = X^{(k)} + \sigma \left(S^{(k+1)} + \mathcal{A}^*y^{(k+1)} - C \right), \tag{24c}$$

with penalty parameter $\sigma > 0$. For large-scale SDPs, the PSD-cone projection $\Pi_{\mathbb{S}_+^n}(\cdot)$ is typically the main computational bottleneck. We therefore replace $\Pi_{\mathbb{S}_+^n}(\cdot)$ with our composite polynomial filtering, implemented in both FP32 and FP16 arithmetic.

Experiment set-up. We choose four large-scale instances from the Mittelmann SDP test set [27] whose matrix dimension is at least 5000: G55mc ($n = 5000$), G59mc ($n = 5000$), G60_mb ($n = 7000$) and G60mc

| | Relative Error | | | Time (s) | | |
|----------------------|-----------------------|-----------------------|-----------------------|-----------------------|-----------------------|-----------------------|
| | Mean | Median | Std. | Mean | Median | Std. |
| cuSOLVER FP64 | 0.00×10^0 | 0.00×10^0 | 0.00×10^0 | 8.85×10^{-1} | 8.77×10^{-1} | 4.47×10^{-2} |
| cuSOLVER FP32 | 1.89×10^{-5} | 4.48×10^{-6} | 4.06×10^{-5} | 5.84×10^{-1} | 5.58×10^{-1} | 5.36×10^{-2} |
| Polar Express FP32 | 1.57×10^{-4} | 5.21×10^{-5} | 3.01×10^{-4} | 1.04×10^0 | 1.01×10^0 | 3.75×10^{-2} |
| Polar Express FP16 | 6.38×10^{-3} | 4.51×10^{-4} | 3.08×10^{-2} | 5.17×10^{-2} | 4.97×10^{-2} | 5.90×10^{-3} |
| Newton-Schulz FP32 | 1.61×10^{-2} | 5.55×10^{-4} | 7.87×10^{-2} | 1.06×10^0 | 1.03×10^0 | 3.79×10^{-2} |
| Newton-Schulz FP16 | 2.65×10^{-2} | 4.22×10^{-3} | 9.08×10^{-2} | 6.09×10^{-2} | 5.98×10^{-2} | 5.33×10^{-3} |
| Composite FP32 (em.) | 4.75×10^{-5} | 9.12×10^{-6} | 7.37×10^{-5} | 4.16×10^{-1} | 4.03×10^{-1} | 7.42×10^{-2} |
| Composite FP16 | 3.45×10^{-3} | 3.70×10^{-4} | 1.42×10^{-2} | 5.48×10^{-2} | 5.45×10^{-2} | 6.41×10^{-3} |

Table 4: Statistics of the PSD projection methods on datasets of size 10000 for B200 GPU.

| | Relative Error | | | Time (s) | | |
|----------------------|-----------------------|-----------------------|-----------------------|-----------------------|-----------------------|-----------------------|
| | Mean | Median | Std. | Mean | Median | Std. |
| cuSOLVER FP64 | 0.00×10^0 | 0.00×10^0 | 0.00×10^0 | 5.13×10^0 | 5.08×10^0 | 2.43×10^{-1} |
| cuSOLVER FP32 | 1.73×10^{-5} | 6.21×10^{-6} | 2.69×10^{-5} | 3.04×10^0 | 2.96×10^0 | 2.02×10^{-1} |
| Polar Express FP32 | 4.08×10^{-4} | 7.45×10^{-5} | 9.46×10^{-4} | 7.84×10^0 | 7.58×10^0 | 2.84×10^{-1} |
| Polar Express FP16 | 1.09×10^{-2} | 4.61×10^{-4} | 5.60×10^{-2} | 2.98×10^{-1} | 2.85×10^{-1} | 4.41×10^{-2} |
| Newton-Schulz FP32 | 1.69×10^{-2} | 5.35×10^{-4} | 8.28×10^{-2} | 7.91×10^0 | 7.64×10^0 | 2.85×10^{-1} |
| Newton-Schulz FP16 | 2.72×10^{-2} | 3.69×10^{-3} | 9.30×10^{-2} | 3.25×10^{-1} | 3.14×10^{-1} | 3.92×10^{-2} |
| Composite FP32 (em.) | 1.21×10^{-4} | 2.36×10^{-5} | 2.16×10^{-4} | 2.99×10^0 | 2.93×10^0 | 5.58×10^{-1} |
| Composite FP16 | 8.59×10^{-3} | 5.14×10^{-4} | 4.30×10^{-2} | 3.01×10^{-1} | 2.91×10^{-1} | 4.42×10^{-2} |

Table 5: Statistics of the PSD projection methods on datasets of size 20000 for B200 GPU.

($n = 7000$). The ADMM iteration limit is fixed at 5000, and the algorithm stops once the maximum KKT residual η falls below 10^{-4} , where

$$\eta := \max \left\{ \frac{\|AX - b\|_2}{1 + \|b\|_2}, \frac{\|A^*y + S - C\|_F}{1 + \|C\|_F}, \frac{|\langle C, X \rangle - b^T y|}{1 + |\langle C, X \rangle| + |b^T y|}, \frac{\min\{0, \lambda_{\min}(X)\}}{1 + \|b\|_2}, \frac{\min\{0, \lambda_{\min}(S)\}}{1 + \|C\|_F} \right\}.$$

The ADMM iterate (24) is warm-started with our composite polynomial filters. Because no eigenvalues are computed explicitly in this phase, we monitor only the quantity $\max \left\{ \frac{\|AX - b\|_2}{1 + \|b\|_2}, \frac{\|A^*y + S - C\|_F}{1 + \|C\|_F}, \frac{|\langle C, X \rangle - b^T y|}{1 + |\langle C, X \rangle| + |b^T y|} \right\}$, using it as a surrogate for η . Once this surrogate first drops below 10^{-2} , we switch to the FP64 PSD-cone projection based on an eigenvalue decomposition.

Results. The results are shown in Figure 3. In every experiment we examine, *a posteriori*, the minimum eigenvalues of the final iterates $X^{(k)}$ and $S^{(k)}$; they remain far below 10^{-8} —even for G60mc in FP32, where the algorithm never switches to the high-precision projection. This confirms that our surrogate for η is adequate. For the two easier instances (G55mc and G59mc) ADMM reduces η below 10^{-4} within 5000 iterations. Across FP64, FP32, and FP16 arithmetic the evolution of η is virtually identical, showing that warming up the first 100 iterations with composite filtering sacrifices almost no accuracy. The harder instances (G60mc and G60_mb) resist pushing η below 10^{-2} . Nevertheless, the FP32 and FP16 projections—although noisier—do not slow convergence. In three of the four problems, low-precision projections actually deliver a smaller final η while reducing the total projection time by up to an order of magnitude. These findings demonstrate that our low-precision projection strategy is both effective and efficient for large-scale semidefinite optimization.

Remark 2. One might question the overall benefit of warm-starting, given that we eventually revert to high-precision projections to obtain higher-accuracy SDP solutions. However, empirical evidence shows that

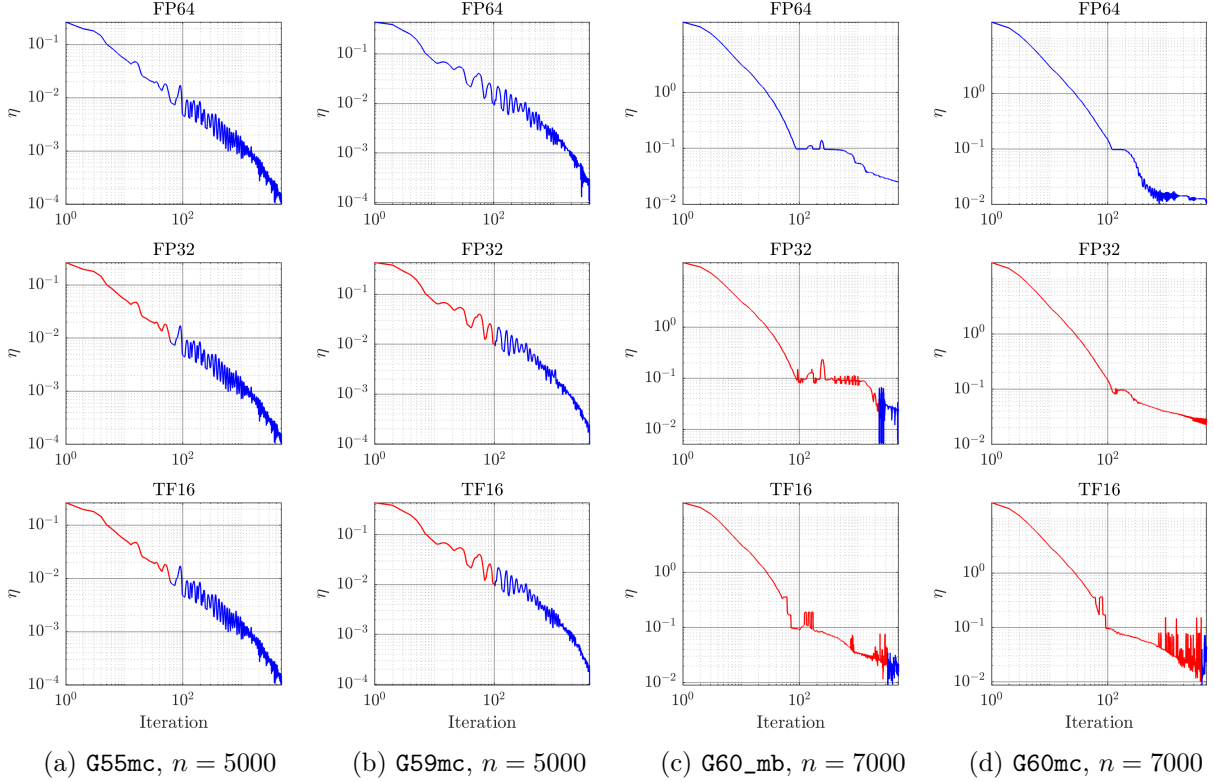


Figure 3: Numerical results for warm-starting ADMM with low-precision PSD-cone projection via composite polynomial filtering. **Red segments**: low-precision projection phase; **blue segments**: high-precision phase. Curves (top to bottom): (1) baseline with purely FP64 projections; (2) warm-start using FP32 composite filtering; (3) warm-start using FP16 composite filtering.

ADMM quickly enters a low-rank regime in which either $X^{(k)}$ or $S^{(k)}$ maintains low rank [19, 37]. In that phase, iterative low-rank eigensolvers such as LOBPCG [23] can perform the PSD projection in nearly $\mathcal{O}(n^2)$ time per iteration. Indeed, an a posteriori inspection of the final $X^{(k)}$ ranks confirms this behavior: (a) G55mc: 53; (b) G59mc: 21; (c) G60_mb: 224 (FP64), 248 (FP32), 178 (FP16); (d) G60mc: 119 (FP64), 298 (FP32), 161 (FP16). Thus, our low-precision projection methods could significantly accelerate entry into this advantageous low-rank regime.

5 Conclusion

We introduced a factorization-free PSD cone projection method that replaces expensive eigenvalue decompositions with a short cascade of low-degree polynomials executed entirely as GEMMs, achieving up to an order-of-magnitude acceleration on NVIDIA B200/H100 GPUs for moderate-accuracy projections. Used as a warm-start within a first-order SDP solver, the filter significantly reduces the total projection time without slowing convergence.

Limitations and future work. Composite filtering excels on dense spectra but can stumble when a few dominant eigenvalues are present; a preliminary deflation step may therefore be required. Future work will explore (i) hybrid variants that couple the polynomial filter with low-rank corrections to cut GEMM counts further, and (ii) adaptive strategies that adjust the polynomial depth online based on real-time spectral estimates.

Acknowledgment

We thank Steven Dalton, Cris Cecka, Samuel Rodriguez Bernabeu, and Mikail Khona at NVIDIA for valuable discussions on numerical linear algebra methods on GPUs. Part of this research was conducted during visits by SK and HY to the Polynomial Optimization team at LAAS-CNRS, where Jean-Bernard Lasserre, Didier Henrion, and Victor Magron provided helpful insights.

A Remez Algorithm

This section provides Remez algorithm’s necessary backgrounds for completeness.

Definition 1 (Minimax approximate polynomial). *Given a continuous function g over a compact interval $[a, b]$ ($a, b > 0$), $f^* \in \mathbb{R}_d^{\text{odd}}[x]$ is called a minimax approximate polynomial, if and only if*

$$f^* = \arg \min_{f \in \mathbb{R}_d^{\text{odd}}[x]} \max_{x \in [a, b]} |f(x) - g(x)| \quad (25)$$

The existence and uniqueness of such an f^* is guaranteed [1, Lemma A.1].

Remez algorithm [35] provides a systematic way to compute such an f^* , as illustrated in Algorithm 3.

Algorithm 3: Remez algorithm [25, Algorithm 1]

Input: The target function g , compact interval $[a, b]$, a set of polynomial basis $\Phi := \{\varphi_\ell\}_{\ell=1}^d$.

Output: The minimax approximate function f^* .

- 1 Initialization of extremal points: $d + 1$ Chebyshev nodes $\{x_i\}_{i=1}^{d+1}$ on $[a, b]$.
 - 2 **for** $k = 1$ **to** ∞ **do**
 - 3 (1) Build and solve the alternation system. The linear system has $d + 1$ variables: $\{c_\ell\}_{\ell=1}^d$ and E . The $d + 1$ linear equations are:

$$\sum_{\ell=1}^d c_\ell \varphi_\ell(x_i) - g(x_i) = (-1)^i E, \quad \forall i = 1, \dots, d + 1.$$
 - 4 (2) Get the d roots $\{z_\ell\}_{\ell=1}^d$ of the residual $e(x) := \sum_{\ell=1}^d c_\ell \varphi_\ell(x) - g(x)$:

$$x_1 < z_1 < x_2 < z_2 < x_3 < \dots < x_{d-1} < z_{d-1} < x_d < z_d < x_{d+1}$$
 - 5 (3) Update the $d + 1$ extremal points. Divide $[a, b]$ into $d + 1$ sub-intervals:

$$[z_0 := a, z_1], [z_1, z_2], \dots, [z_{d-1}, z_d], [z_d, z_{d+1} := b]$$

For each sub-interval $[z_{i-1}, z_i]$ ($i = 1, \dots, d + 1$), find the maximum (resp. minimum) point of $e(x)$ if $e(x_i)$ is positive (resp. negative). Denote these $d + 1$ extremal points as $\{y_i\}_{i=1}^{d+1}$.
 - 6 (4) Check convergence. If $\{y_i\}_{i=1}^{d+1}$ is sufficiently close to $\{x_i\}_{i=1}^{d+1}$, break. Else, replace $\{x_i\}_{i=1}^{d+1}$ with $\{y_i\}_{i=1}^{d+1}$.
 - 7 **end**
-

B Complete Comparison of PSD Projection Methods

This section provides the complete results of the comparison of the different PSD projection methods, including the relative error and execution time of each method on each dataset for both GPU architectures (H100 and B200). Tables 6, 7, and 8 show the results for the H100 GPU aggregated over the datasets. Figures 4 and 5 show the same results in boxplot format. Figures 6 and 7 show the execution time of each method on the B200 and H100 GPUs, separating the different datasets. Figures 8 and 9 show the relative error of each method on the B200 and H100 GPUs per dataset.

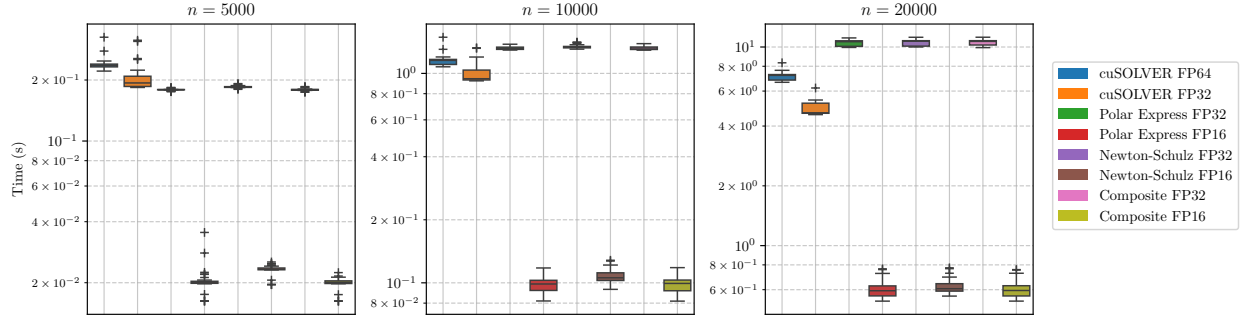


Figure 4: Boxplots for different PSD cone projection methods' *execution time* on H100 GPU.

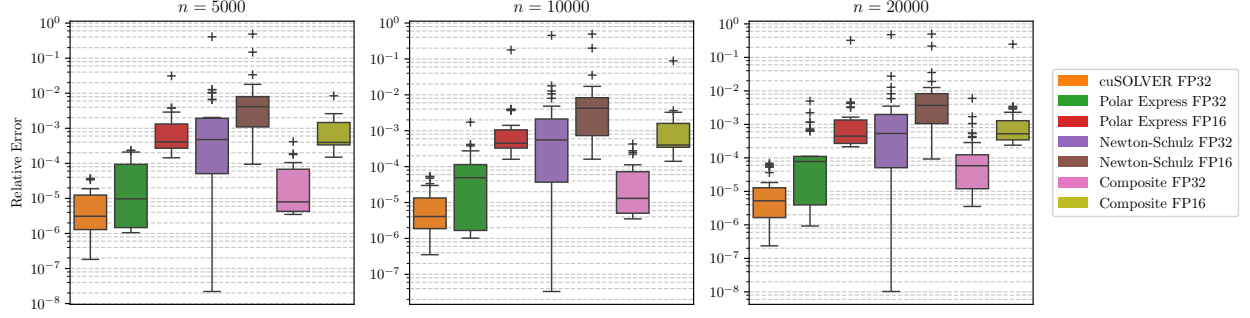


Figure 5: Boxplots for different PSD cone projection methods' *relative error* on H100 GPU.

| | Relative Error | | | Time (s) | | |
|--------------------|-----------------------|-----------------------|-----------------------|-----------------------|-----------------------|-----------------------|
| | Mean | Median | Std. | Mean | Median | Std. |
| cuSOLVER FP64 | 0.00×10^0 | 0.00×10^0 | 0.00×10^0 | 2.38×10^{-1} | 2.36×10^{-1} | 1.88×10^{-2} |
| cuSOLVER FP32 | 7.96×10^{-6} | 3.10×10^{-6} | 1.06×10^{-5} | 2.05×10^{-1} | 1.93×10^{-1} | 3.28×10^{-2} |
| Polar Express FP32 | 5.43×10^{-5} | 9.70×10^{-6} | 7.31×10^{-5} | 1.79×10^{-1} | 1.79×10^{-1} | 1.85×10^{-3} |
| Polar Express FP16 | 1.83×10^{-3} | 4.08×10^{-4} | 5.38×10^{-3} | 2.06×10^{-2} | 2.01×10^{-2} | 3.34×10^{-3} |
| Newton-Schulz FP32 | 1.47×10^{-2} | 4.77×10^{-4} | 7.07×10^{-2} | 1.85×10^{-1} | 1.85×10^{-1} | 2.42×10^{-3} |
| Newton-Schulz FP16 | 2.49×10^{-2} | 4.14×10^{-3} | 8.70×10^{-2} | 2.32×10^{-2} | 2.33×10^{-2} | 1.38×10^{-3} |
| Composite FP32 | 4.93×10^{-5} | 7.95×10^{-6} | 8.21×10^{-5} | 1.79×10^{-1} | 1.79×10^{-1} | 2.51×10^{-3} |
| Composite FP16 | 1.05×10^{-3} | 3.95×10^{-4} | 1.50×10^{-3} | 1.99×10^{-2} | 2.01×10^{-2} | 1.39×10^{-3} |

Table 6: Statistics of the PSD projection methods on datasets of size 5000 for H100 GPU.

| | Relative Error | | | Time (s) | | |
|--------------------|-----------------------|-----------------------|-----------------------|-----------------------|-----------------------|-----------------------|
| | Mean | Median | Std. | Mean | Median | Std. |
| cuSOLVER FP64 | 0.00×10^0 | 0.00×10^0 | 0.00×10^0 | 1.16×10^0 | 1.15×10^0 | 7.47×10^{-2} |
| cuSOLVER FP32 | 1.08×10^{-5} | 4.07×10^{-6} | 1.53×10^{-5} | 1.00×10^0 | 9.43×10^{-1} | 1.04×10^{-1} |
| Polar Express FP32 | 1.34×10^{-4} | 4.91×10^{-5} | 3.09×10^{-4} | 1.32×10^0 | 1.32×10^0 | 2.43×10^{-2} |
| Polar Express FP16 | 6.37×10^{-3} | 4.47×10^{-4} | 3.08×10^{-2} | 9.81×10^{-2} | 9.87×10^{-2} | 8.67×10^{-3} |
| Newton-Schulz FP32 | 1.61×10^{-2} | 5.54×10^{-4} | 7.87×10^{-2} | 1.34×10^0 | 1.34×10^0 | 2.70×10^{-2} |
| Newton-Schulz FP16 | 2.65×10^{-2} | 4.23×10^{-3} | 9.07×10^{-2} | 1.08×10^{-1} | 1.06×10^{-1} | 8.49×10^{-3} |
| Composite FP32 | 6.20×10^{-5} | 1.31×10^{-5} | 9.72×10^{-5} | 1.32×10^0 | 1.32×10^0 | 2.69×10^{-2} |
| Composite FP16 | 3.64×10^{-3} | 4.00×10^{-4} | 1.52×10^{-2} | 9.82×10^{-2} | 9.93×10^{-2} | 8.90×10^{-3} |

Table 7: Statistics of the PSD projection methods on datasets of size 10000 for H100 GPU.

| | Relative Error | | | Time (s) | | |
|--------------------|-----------------------|-----------------------|-----------------------|-----------------------|-----------------------|-----------------------|
| | Mean | Median | Std. | Mean | Median | Std. |
| cuSOLVER FP64 | 0.00×10^0 | 0.00×10^0 | 0.00×10^0 | 7.14×10^0 | 7.20×10^0 | 3.21×10^{-1} |
| cuSOLVER FP32 | 1.42×10^{-5} | 5.21×10^{-6} | 2.09×10^{-5} | 4.91×10^0 | 4.66×10^0 | 3.73×10^{-1} |
| Polar Express FP32 | 4.01×10^{-4} | 7.80×10^{-5} | 9.50×10^{-4} | 1.05×10^1 | 1.06×10^1 | 3.70×10^{-1} |
| Polar Express FP16 | 1.08×10^{-2} | 4.45×10^{-4} | 5.60×10^{-2} | 6.03×10^{-1} | 5.93×10^{-1} | 6.06×10^{-2} |
| Newton-Schulz FP32 | 1.68×10^{-2} | 5.34×10^{-4} | 8.28×10^{-2} | 1.05×10^1 | 1.07×10^1 | 3.99×10^{-1} |
| Newton-Schulz FP16 | 2.68×10^{-2} | 3.69×10^{-3} | 9.24×10^{-2} | 6.22×10^{-1} | 6.07×10^{-1} | 5.32×10^{-2} |
| Composite FP32 | 3.61×10^{-4} | 5.82×10^{-5} | 1.07×10^{-3} | 1.05×10^1 | 1.07×10^1 | 3.84×10^{-1} |
| Composite FP16 | 8.49×10^{-3} | 5.25×10^{-4} | 4.30×10^{-2} | 6.04×10^{-1} | 5.94×10^{-1} | 6.02×10^{-2} |

Table 8: Statistics of the PSD projection methods on datasets of size 20000 for H100 GPU.

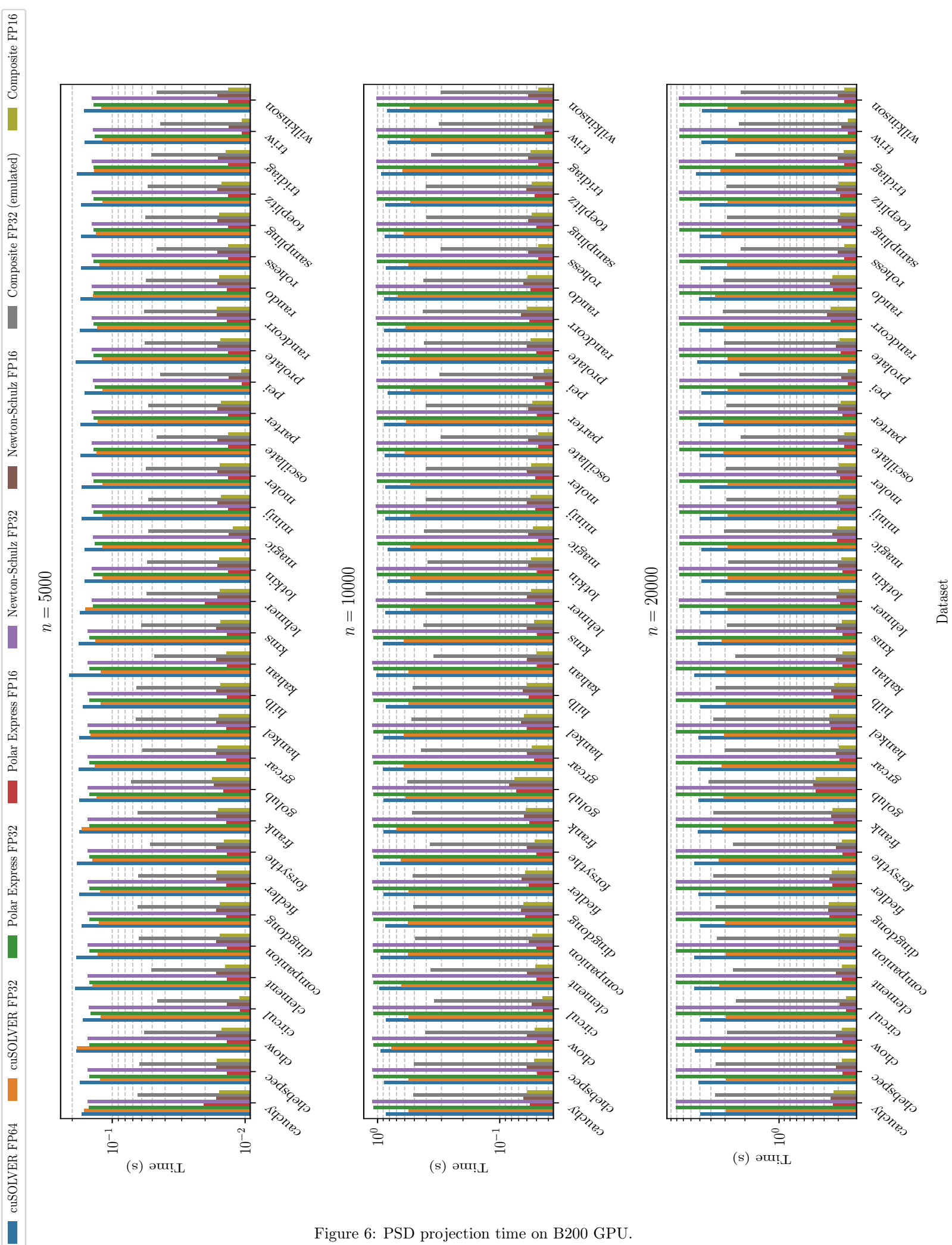


Figure 6: PSD projection time on B200 GPU.

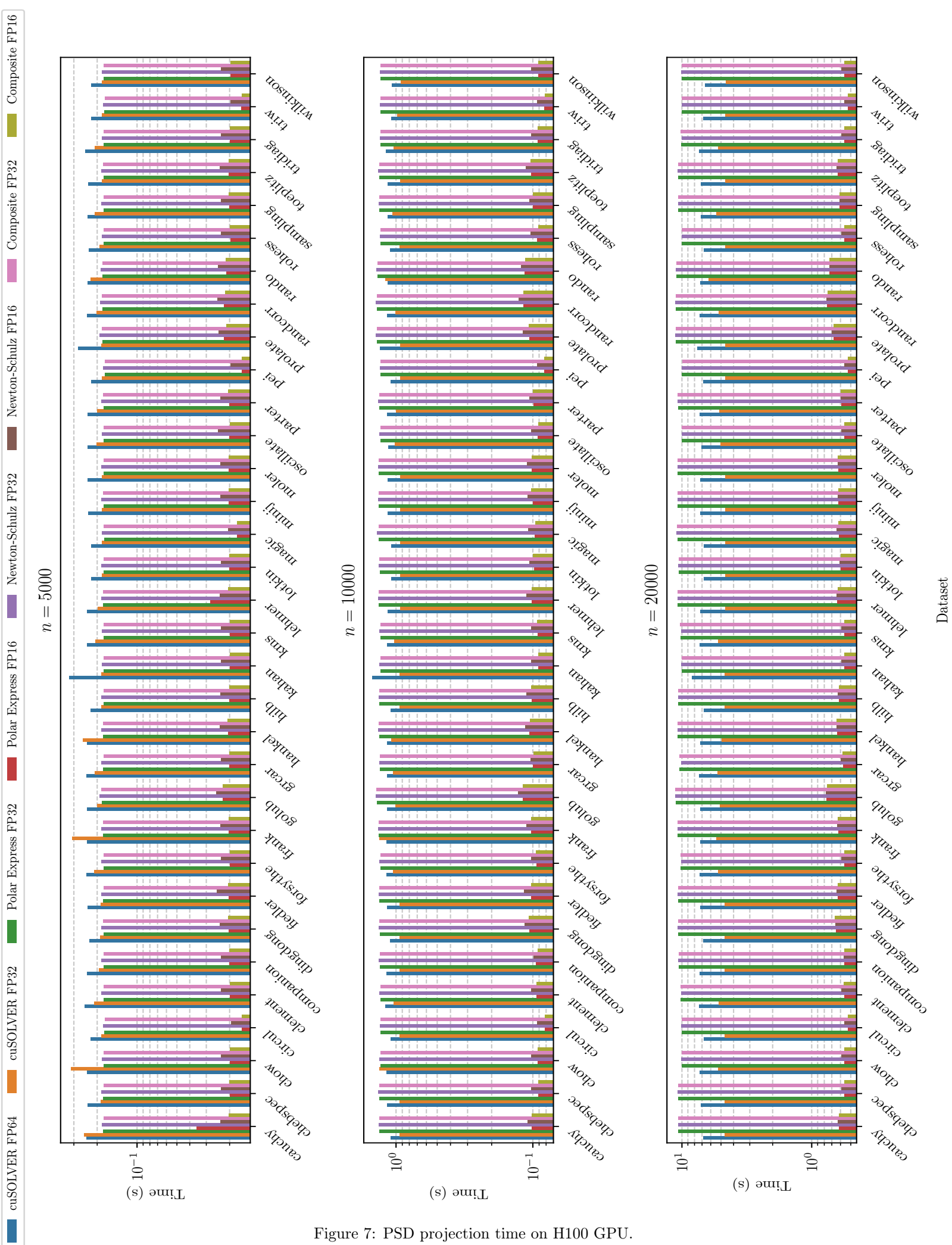


Figure 7: PSD projection time on H100 GPU.

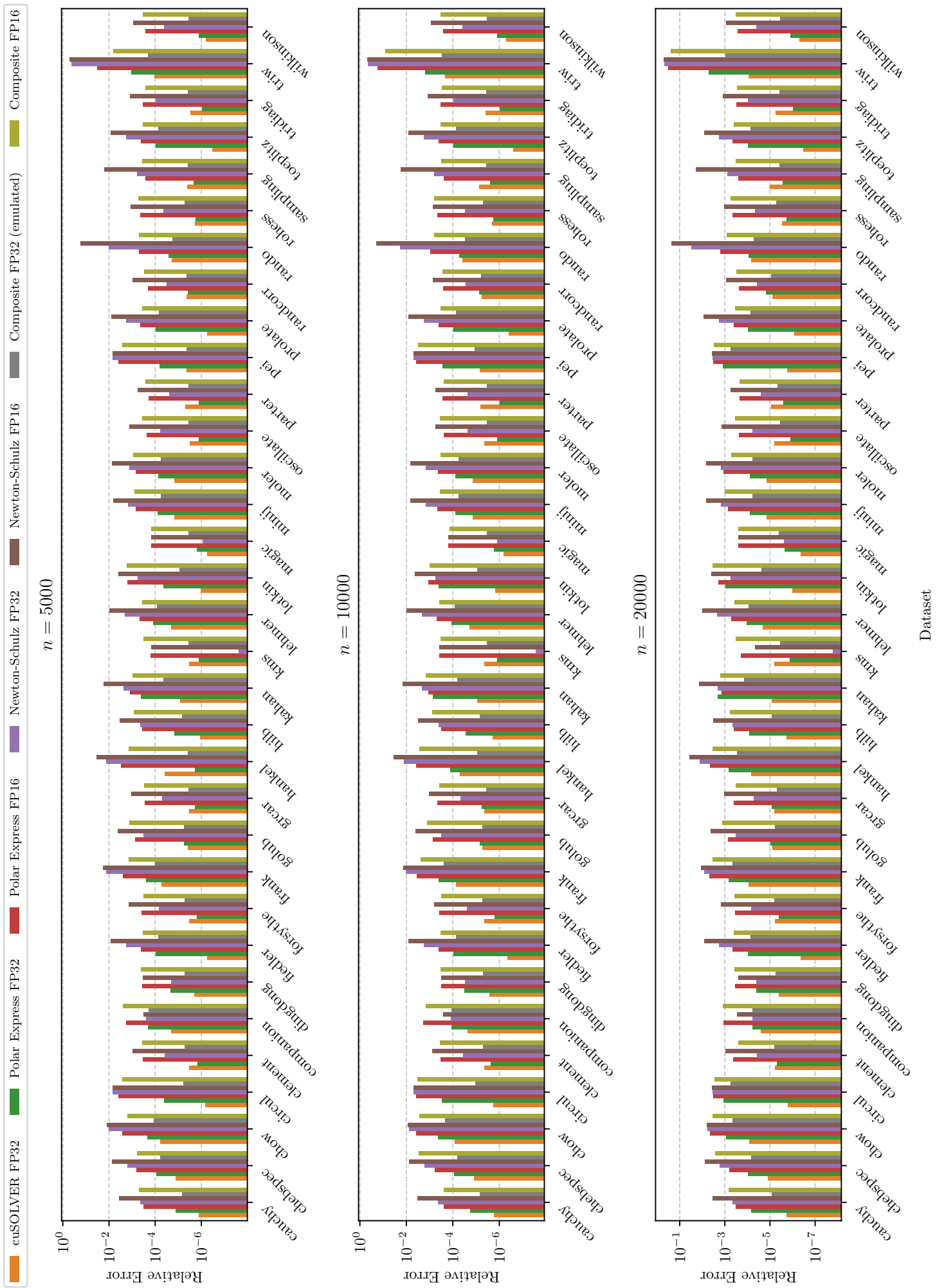


Figure 8: PSD projection error on B200 GPU.

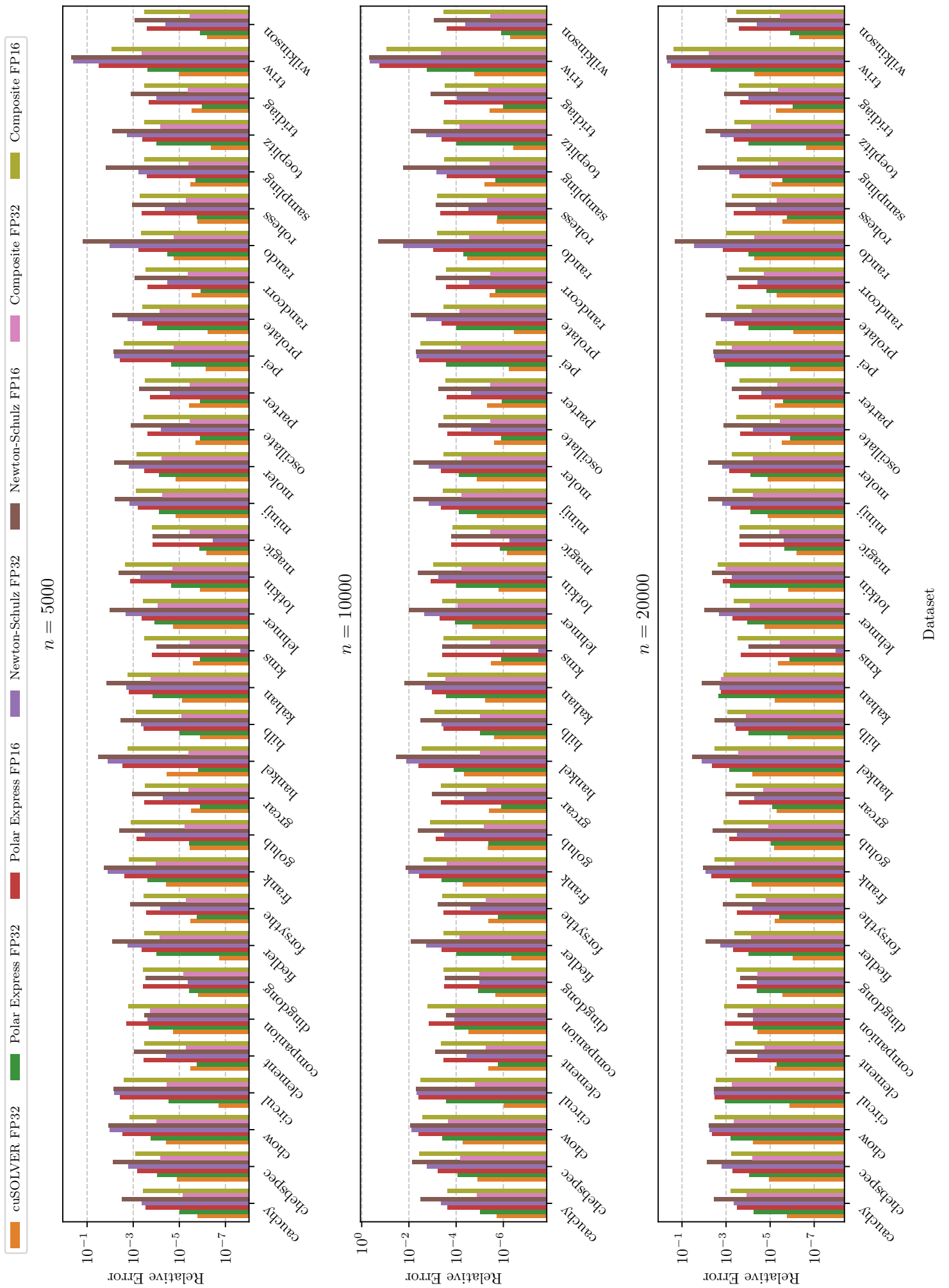


Figure 9: PSD projection error on H100 GPU.

References

- [1] Noah Amsel, David Persson, Christopher Musco, and Robert Gower. The polar express: Optimal matrix sign methods and their application to the muon algorithm. *arXiv preprint arXiv:2505.16932*, 2025.
- [2] Edward Anderson, Zhaojun Bai, Christian Bischof, L Susan Blackford, James Demmel, Jack Dongarra, Jeremy Du Croz, Anne Greenbaum, Sven Hammarling, Alan McKenney, et al. *LAPACK users' guide*. SIAM, 1999.
- [3] Júlia Barberà-Rodríguez, Leonardo Zambrano, Antonio Acín, and Donato Farina. Boosting projective methods for quantum process and detector tomography. *Physical Review Research*, 7:013208, 2025.
- [4] Franz Louis Cesista, YouJiacheng, and Keller Jordan. Squeezing 1-2% efficiency gains out of Muon by optimizing the Newton-Schulz coefficients. <https://leloykun.github.io/ponder/muon-opt-coeffs/>, 2024. Accessed: 2025-06-29.
- [5] Jie Chen and Edmond Chow. A stable scaling of Newton-Schulz for improving the sign function computation of a hermitian matrix. Technical Report ANL/MCS-P5059-0114, Argonne National Laboratory, 2014.
- [6] Eugene D. Denman and Alex N. Beavers. The matrix sign function and computations in systems. *Applied Mathematics and Computation*, 2(1):63–94, 1976.
- [7] Chao Ding, Defeng Sun, Jie Sun, and Kim-Chuan Toh. Spectral operators of matrices. *Mathematical Programming*, 168:509–531, 2018.
- [8] Dmitriy Drusvyatskiy, Chi-Kwong Li, Diane C. Pelejo, Yuen-Lam Voronin, and Henry Wolkowicz. Projection methods for quantum channel construction. *Quantum Information Processing*, 14:3075–3096, 2015.
- [9] Juliano B. Francisco and Douglas S. Gonçalves. A fixed-point method for approximate projection onto the positive semidefinite cone. *Linear Algebra and its Applications*, 523:59–78, 2017.
- [10] Michael Garstka, Mark Cannon, and Paul Goulart. Cosmo: A conic operator splitting method for convex conic problems. *Journal of Optimization Theory and Applications*, 190(3):779–810, 2021.
- [11] Federico Girosi and Tomaso Poggio. Networks and the best approximation property. *Biological Cybernetics*, 63(3):169–176, 1990.
- [12] Abdulla Haidar, Stanimire Tomov, Ichitaro Yamazaki, Romain Solca, Thomas Schulthess, Tingxing Dong, and Jack Dongarra. MAGMA: A breakthrough in solvers for eigenvalue problems. White paper, GPU Technology Conference (GTC'12), May 2012.
- [13] Haoyu Han and Heng Yang. Building rome with convex optimization. In *Robotics: Science and Systems (RSS)*, 2025.
- [14] Nicholas J. Higham. Computing the polar decomposition—with applications. *SIAM Journal on Scientific and Statistical Computing*, 7(4):1160–1174, 1986.
- [15] Nicholas J Higham. Computing a nearest symmetric positive semidefinite matrix. *Linear algebra and its applications*, 103:103–118, 1988.
- [16] Nicholas J. Higham. Computing the nearest correlation matrix—a problem from finance. *IMA Journal of Numerical Analysis*, 22(3):329–343, 2002.
- [17] Nicholas J. Higham. *Functions of Matrices: Theory and Computation*. Society for Industrial and Applied Mathematics, Philadelphia, PA, 2008.

- [18] Morgan Jones and James Anderson. Approximate projections onto the positive semidefinite cone using randomization. *arXiv preprint arXiv:2410.19208*, 2024.
- [19] Shucheng Kang, Xin Jiang, and Heng Yang. Local linear convergence of the alternating direction method of multipliers for semidefinite programming under strict complementarity. *arXiv preprint arXiv:2503.20142*, 2025.
- [20] Shucheng Kang, Guorui Liu, and Heng Yang. Global contact-rich planning with sparsity-rich semidefinite relaxations. In *Robotics: Science and Systems (RSS)*, 2025.
- [21] Shucheng Kang, Xiaoyang Xu, Jay Sarva, Ling Liang, and Heng Yang. Fast and certifiable trajectory optimization. In *International Workshop on the Algorithmic Foundations of Robotics (WAFR)*, 2024.
- [22] Igor Klep, Victor Magron, Jurij Volčič, and Jie Wang. State polynomials: positivity, optimization and nonlinear bell inequalities. *Mathematical Programming*, 207(1):645–691, 2024.
- [23] Andrew V. Knyazev. Toward the optimal preconditioned eigensolver: Locally optimal block preconditioned conjugate gradient method. *SIAM Journal on Scientific Computing*, 23(2):517–541, 2001.
- [24] Jean B Lasserre. Min-max and robust polynomial optimization. *Journal of Global Optimization*, 51(1):1–10, 2011.
- [25] Eunsang Lee, Joon Woo Lee, Jong Seon No, and Young Sik Kim. Minimax approximation of sign function by composite polynomial for homomorphic comparison. *IEEE Transactions on Dependable and Secure Computing*, 19(6):3711–3727, 2022.
- [26] Victor Magron and Jie Wang. *Sparse polynomial optimization: theory and practice*. World Scientific, 2023.
- [27] Hans D Mittelmann. Several sdp-codes on sparse and other sdp problems, 2006.
- [28] Yuji Nakatsukasa, Zhaojun Bai, and François Gygis. Optimizing Halley’s iteration for computing the matrix polar decomposition. *SIAM Journal on Matrix Analysis and Applications*, 31(5):2700–2720, 2010.
- [29] NVIDIA Corporation. *NVIDIA A100 Tensor Core GPU Architecture*, 2020. Whitepaper.
- [30] NVIDIA Corporation. Boosting matrix multiplication speed and flexibility with nvidia cublas 12.9. <https://developer.nvidia.com/blog/boosting-matrix-multiplication-speed-and-flexibility-with-nvidia-cublas-12-9/>, May 2024. Accessed: 2025-06-14.
- [31] NVIDIA Corporation. *NVIDIA cuSOLVER Library*, 2024. Version 12.x.
- [32] NVIDIA Corporation. *cuBLAS Library User Guide, Version 12.9*, 2025. NVIDIA Developer Documentation.
- [33] Brendan O’Donoghue, Eric Chu, Neal Parikh, and Stephen Boyd. SCS: Splitting conic solver, version 3.2.4. <https://github.com/cvxgrp/scs>, November 2023.
- [34] Beresford N Parlett. *The symmetric eigenvalue problem*. SIAM, Philadelphia, PA, 1998.
- [35] E. Ya. Remez. *General Computational Methods of Chebyshev Approximation: The Problems with Linear Realization*. Kiev: Izdatel’stvo Akademii Nauk Ukrainskoi SSR, 1962. In Russian; English translation by J. H. McCabe, 1964, U.S. Department of Commerce, Office of Technical Services.
- [36] Nikitas Rontsis, Paul Goulart, and Yuji Nakatsukasa. Efficient semidefinite programming with approximate ADMM. *Journal of Optimization Theory and Applications*, pages 1–29, 2022.

- [37] Mario Souto, Joaquim D Garcia, and Álvaro Veiga. Exploiting low-rank structure in semidefinite programming by approximate operator splitting. *Optimization*, 71(1):117–144, 2022.
- [38] Stanimire Tomov, Jack Dongarra, and Marc Baboulin. Towards dense linear algebra for hybrid GPU accelerated manycore systems. *Parallel Computing*, 36(5-6):232–240, 2010.
- [39] Lloyd N Trefethen. *Approximation theory and approximation practice, extended edition*. SIAM, 2019.
- [40] Vasily Volkov and James W. Demmel. Benchmarking GPUs to tune dense linear algebra. In *Proceedings of the 2008 ACM/IEEE Conference on Supercomputing (SC’08)*, pages 1–11. IEEE, 2008.
- [41] Jie Wang, Jacopo Surace, Irénée Frérot, Benoît Legat, Marc-Olivier Renou, Victor Magron, and Antonio Acín. Certifying ground-state properties of quantum many-body systems. *Physical Review X*, 2024.
- [42] Kilian Q. Weinberger and Lawrence K. Saul. Distance metric learning for large margin nearest neighbor classification. *Journal of Machine Learning Research*, 10:207–244, 2009.
- [43] Zaiwen Wen, Donald Goldfarb, and Wotao Yin. Alternating direction augmented Lagrangian methods for semidefinite programming. *Mathematical Programming Computation*, 2(3):203–230, 2010.
- [44] Samuel Williams, Andrew Waterman, and David Patterson. Roofline: An insightful visual performance model for multicore architectures. *Communications of the ACM*, 52(4):65–76, 2009.
- [45] Heng Yang, Ling Liang, Luca Carlone, and Kim-Chuan Toh. An inexact projected gradient method with rounding and lifting by nonlinear programming for solving rank-one semidefinite relaxation of polynomial optimization. *Mathematical Programming*, 201(1):409–472, 2023.
- [46] L Minah Yang, Alyson Fox, and Geoffrey Sanders. Rounding error analysis of mixed precision block Householder QR algorithms. *SIAM Journal on Scientific Computing*, 43(3):A1723–A1753, 2021.
- [47] Liuqin Yang, Defeng Sun, and Kim-Chuan Toh. SDPNAL+: A majorized semismooth Newton-CG augmented Lagrangian method for semidefinite programming with nonnegative constraints. *Mathematical Programming Computation*, 7(3):331–366, 2015.
- [48] Tianyu Yang, Mahdi Barzegar Khalilsarai, Saeid Haghighatshoar, and Giuseppe Caire. Structured channel covariance estimation from limited samples for large antenna arrays. *EURASIP Journal on Wireless Communications and Networking*, 2023(24):1–34, 2023.
- [49] Weijian Zhang and Nicholas J Higham. Matrix depot: an extensible test matrix collection for julia. *PeerJ Computer Science*, 2:e58, 2016.
- [50] Yang Zheng, Giovanni Fantuzzi, Antonis Papachristodoulou, Paul Goulart, and Andrew Wynn. Fast ADMM for homogeneous self-dual embedding of sparse SDPs. *IFAC-PapersOnLine*, 50(1):8411–8416, 2017.
- [51] Åke Björck and Charles Bowie. An iterative algorithm for computing the best estimate of an orthogonal matrix. *SIAM Journal on Numerical Analysis*, 8(2):358–364, 1971.